

# Lightning over the Boreal Zone: Skill Assessment for Various Land-Atmosphere Model Configurations and Lightning Indices

Jonas Mortelmans<sup>1,1</sup>, Michel Bechtold<sup>1,1</sup>, Erwan Brisson<sup>2,2</sup>, Barry Hugh Lynn<sup>3,3</sup>, Sujay Kumar<sup>4,4</sup>, and Gabrielle J.M. De Lannoy<sup>5,5</sup>

<sup>1</sup>KU Leuven

<sup>2</sup>Goethe University Frankfurt

<sup>3</sup>Hebrew University of Jerusalem

<sup>4</sup>NASA GSFC

<sup>5</sup>KU Leuven, Department of Earth and Environmental Sciences

November 30, 2022

## Abstract

Current lightning predictions are uncertain because they either rely on empirical diagnostic relationships based on the present climate or use coarse-scale climate scenario simulations in which deep convection is parameterized. Previous studies demonstrated that simulations with convection-permitting resolutions (km-scale) improve lightning predictions compared to coarser-grid simulations using convection parameterization for different geographical locations but not over the boreal zone.

In this study, lightning simulations with the NASA Unified-Weather Research and Forecasting (NU-WRF) model are evaluated over a 955x540 km<sup>2</sup> domain including the Great Slave Lake in Canada for six lightning seasons. The simulations are performed at convection-parameterized (9 km) and convection-permitting (3 km) resolution using the Goddard 4ICE and the Thompson microphysics (MP) schemes. Four lightning indices are evaluated against observations from the Canadian Lightning Detection Network (CLDN), in terms of spatiotemporal frequency distribution, spatial pattern, daily climatology, and an event-based overall skill assessment. Concerning the model configuration, regardless of the spatial resolution, the Thompson scheme is superior to the Goddard 4ICE scheme in predicting the daily climatology but worse in predicting the spatial patterns of lightning occurrence. Several evaluation metrics indicate the benefit of working at a convection-permitting resolution. The relative performance of the different lightning indices depends on the evaluation criteria. Finally, this study demonstrates issues of the models to reproduce the observed spatial pattern of lightning well, which might be related to an insufficient representation of land surface heterogeneity in the study area.

1 **Lightning over the Boreal Zone: Skill Assessment for**  
2 **Various Land-Atmosphere Model Configurations and**  
3 **Lightning Indices**

4 **Jonas Mortelmans<sup>1</sup>, Michel Bechtold<sup>1</sup>, Erwan Brisson<sup>2</sup>, Barry Lynn<sup>3</sup>, Sujay**  
5 **Kumar<sup>4</sup>, Gabriëlle De Lannoy<sup>1</sup>**

6 <sup>1</sup>Department of Earth and Environmental Sciences, KU Leuven, Heverlee, B-3001, Belgium

7 <sup>2</sup>Centre National de la Recherche Scientifique, Toulouse, France

8 <sup>3</sup>Department of Earth Sciences, The Hebrew University of Jerusalem, Givat Ram, Jerusalem 9190401,  
9 Israel; Weather It Is, Ltd., Jerusalem 9134401, Israel

10 <sup>4</sup>Hydrological Science Laboratory, NASA Goddard Space Flight Center, Greenbelt, MD, USA

11 **Key Points:**

- 12 • The NU-WRF modeling framework is run at two resolutions to predict lightning  
13 over the boreal zone for the first time.  
14 • The simulations at the convection-permitting resolution yield more accurate light-  
15 ning predictions.

---

Corresponding author: Jonas Mortelmans, [Jonas.mortelmans@kuleuven.be](mailto:Jonas.mortelmans@kuleuven.be)

16 **Abstract**

17 Current lightning predictions are uncertain because they either rely on empirical  
18 diagnostic relationships based on the present climate or use coarse-scale climate scenario  
19 simulations in which deep convection is parameterized. Previous studies demonstrated  
20 that simulations with convection-permitting resolutions (km-scale) improve lightning pre-  
21 dictions compared to coarser-grid simulations using convection parameterization for dif-  
22 ferent geographical locations but not over the boreal zone.

23 In this study, lightning simulations with the NASA Unified-Weather Research and  
24 Forecasting (NU-WRF) model are evaluated over a 955x540 km<sup>2</sup> domain including the  
25 Great Slave Lake in Canada for six lightning seasons. The simulations are performed at  
26 convection-parameterized (9 km) and convection-permitting (3 km) resolution using the  
27 Goddard 4ICE and the Thompson microphysics (MP) schemes. Four lightning indices  
28 are evaluated against observations from the Canadian Lightning Detection Network (CLDN),  
29 in terms of spatiotemporal frequency distribution, spatial pattern, daily climatology, and  
30 an event-based overall skill assessment. Concerning the model configuration, regardless  
31 of the spatial resolution, the Thompson scheme is superior to the Goddard 4ICE scheme  
32 in predicting the daily climatology but worse in predicting the spatial patterns of light-  
33 ning occurrence. Several evaluation metrics indicate the benefit of working at a convection-  
34 permitting resolution. The relative performance of the different lightning indices depends  
35 on the evaluation criteria. Finally, this study demonstrates issues of the models to re-  
36 produce the observed spatial pattern of lightning well, which might be related to an in-  
37 sufficient representation of land surface heterogeneity in the study area.

38 **1 Introduction**

39 The boreal zone consists of a mosaic of different land cover types, mainly forests  
40 and peatlands, both storing large amounts of carbon (Turetsky et al., 2015; Scharlemann  
41 et al., 2014). One of the natural features shaping the boreal landscape is wildfire (Bowman  
42 et al., 2009). Several studies indicate that lightning is the major source of ignition of wild-  
43 fires in the boreal zone (Turetsky et al., 2015). It is proposed that lightning may increase  
44 due to global warming (Flannigan et al., 2013; Loisel et al., 2021; Veraverbeke et al., 2017;  
45 Krawchuk et al., 2009; Wotton et al., 2010), threatening the carbon pools above (forests)  
46 and below (peatlands) the ground by possibly shifting wildfire regimes.

47 Until the last decade, most lightning predictions are challenged by (i) the coarse-  
48 scale resolution of climate simulations in which the critical process of deep convection  
49 is parameterized and the detailed representation of land-atmosphere processes is lack-  
50 ing (Prein et al., 2015; Weisman et al., 1997), and (ii) the use of empirical relationships  
51 between uncertain atmospheric variables and lightning, based on the present climate. How-  
52 ever, in the last decade, the focus of lightning simulations shifted from the coarse-scale  
53 (100 - 10 km) global and regional models to convection-permitting models, operating at  
54 a spatial resolution of less than 4 km (Prein et al., 2015). These finer resolution mod-  
55 els allow for deep convection to be resolved explicitly, resulting in an improved repre-  
56 sentation of most convection related processes (Brisson et al., 2016; Prein et al., 2015;  
57 Lucas-Picher et al., 2021). At the fine resolution, convection parameterization schemes  
58 become obsolete and other processes contributing to deep convection, such as microphys-  
59 ical (MP) processes, and their formulations become more important (Adams-Selin et al.,  
60 2013). The finer spatial resolution of convection-permitting models also allows to rep-  
61 resent more accurately the effect of land surface heterogeneities in the modeled land-atmosphere  
62 interactions (Vanden Broucke & Van Lipzig, 2017).

63 Lightning is the result of a process known as non-inductive charging (Reynolds et  
64 al., 1957; Takahashi, 1978). This mechanism implies electric charge separation due to  
65 rebounding collisions between graupel particles and cloud ice crystals in the presence of

66 supercooled liquid water (Mason & Dash, 2000). This process mainly occurs when there  
 67 is high convective activity in the area. It is thus not surprising that the estimation of  
 68 lightning occurrence via lightning indices, is based on atmospheric variables that control  
 69 convective activity (Finney et al., 2018; Romps et al., 2014). All proposed lightning  
 70 indices have in common that they are diagnostic in nature and, thus, strongly depend  
 71 on the accuracy of the representation of the relevant atmospheric input variables. This  
 72 representation is expected to improve when working at a finer resolution (Brisson et al.,  
 73 2016). However, to date the difference between working at a convection-permitting and  
 74 convection-parameterized resolution is barely investigated with a focus on lightning indices  
 75 and a systematic evaluation of different lightning indices is lacking completely over  
 76 the boreal zone.

77 This study aims to answer the following questions with a focus on a study domain  
 78 in the Canadian boreal zone: (i) What is the difference in performance between lightning  
 79 simulations at the convection-permitting and convection-parameterized resolution?  
 80 (ii) Since various atmospheric model processes are better resolved at convection-permitting  
 81 resolution, what is the impact of the MP scheme on lightning indices? (iii) Since no lightning  
 82 index was specifically developed for the boreal zone, which commonly used lightning  
 83 index performs best in predicting lightning? To answer these questions, the NASA  
 84 Unified-Weather Research and Forecasting (NU-WRF) framework is run with four different  
 85 model configurations using two generally well-performing MP schemes, the Goddard  
 86 4ICE scheme (W. K. Tao et al., 2014) and the Thompson scheme (Thompson et al., 2008),  
 87 at both a convection-parameterized and convection-permitting resolution. Four  
 88 established lightning indices are diagnosed from the different atmospheric simulation outputs  
 89 and evaluated against lightning observations.

90 This paper is organized as follows. In section 2, the model configurations, lightning  
 91 indices, and evaluation procedures are discussed in detail. Section 3 presents and discusses  
 92 the simulation results and the evaluation against observations. Lastly, in section  
 93 4, the main conclusions of this study are given and research needs are discussed.

## 94 **2 Methodology**

### 95 **2.1 Study Domain and Period**

96 The study domain is chosen in a region with dominantly forests and peatland, around  
 97 the Great Slave Lake in Canada, shown by the red rectangle of approximately 550,000 km<sup>2</sup>  
 98 in Figure 1a. This area is characterized by frequent lightning with critical importance  
 99 for wildfire ignition (Veraverbeke et al., 2017). The study domain is embedded within  
 100 two nested simulation domains, using the limited-area approach. The outer (WRF9, full  
 101 extent of Figure 1) and inner (WRF3, white rectangle of Figure 1) domains have a spatial  
 102 resolution of 9 and 3 km and a temporal resolution of 36 and 12 s, respectively. The  
 103 double nested scheme follows the recommendations for spatial spin-up as described in  
 104 Brisson et al. (2016); Prein et al. (2013) and allows for a study area within WRF3 for  
 105 which convection-parameterized (9 km) and convection-permitting (3 km) model simulations  
 106 are performed and compared.

107 Figures 1b-e show the local topography, Moderate Resolution Imaging Spectroradiometer  
 108 (MODIS) land use, and National Centers for Environmental Prediction (NCEP) surface albedo  
 109 and greenness fraction of the study domain at 3 km resolution. This data is used,  
 110 among others, as input by the land component of the coupled land-atmosphere  
 111 simulations.

112 The simulations cover six lightning seasons, i.e. the months June through August  
 113 for the years 2015 through 2020 as these months are known for their high lightning activity  
 114 in the region of interest (Burrows & Kochtubajda, 2010). For this study, these years  
 115 are chosen because of an improved network of lightning sensors. For the spin-up of the

116 land-component, a 10-year long cold-start spin-up was defined before the start of the light-  
 117 ning season in 2015. The spin-up for the following lightning seasons were started from  
 118 the end of the spin-up of the previous lightning season. To also provide a short-term spin-  
 119 up for the coupled L-A run, the model is started 17 days before the actual start of the  
 120 lightning season. This 17-day period is considered sufficient for the spin-up of the atmo-  
 121 spheric model (Z. Tao et al., 2020).

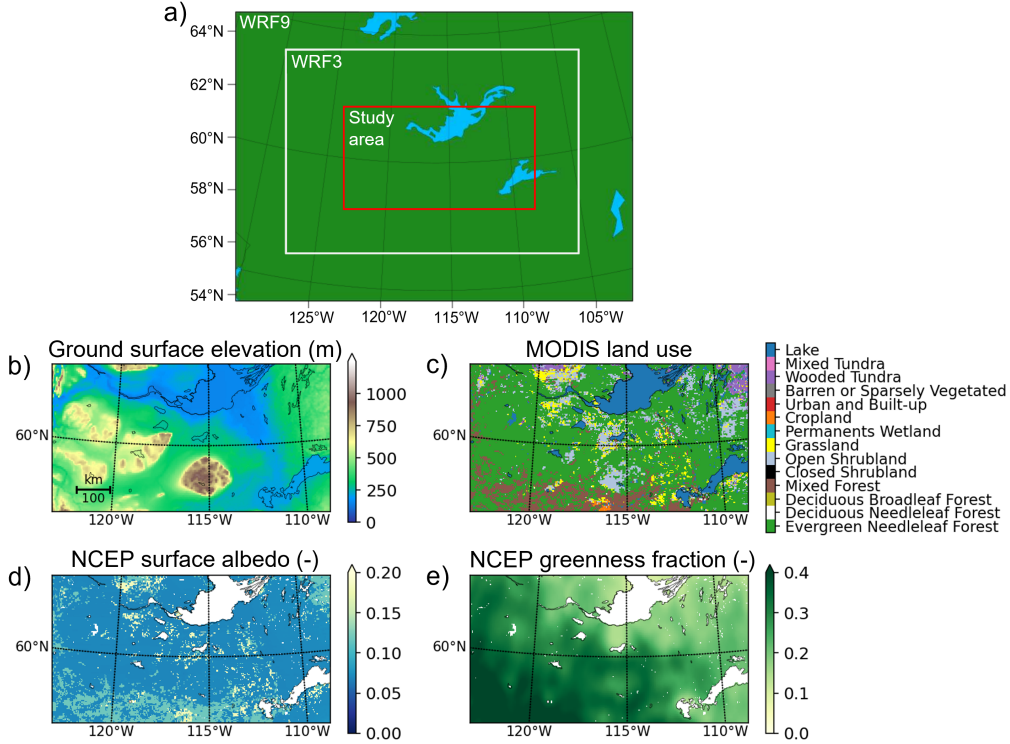


**Figure 1.** (a) The NU-WRF nested domains and study area (red) and its (b) topography (m), (c) MODIS land use, (d) NCEP surface albedo, and (e) NCEP greenness fraction that is used as input for the NU-WRF simulations.

122

## 2.2 Coupled Land-Atmosphere Model Configuration

123

124

125

126

127

128

129

130

131

132

133

134

135

The NU-WRF model is one of the leading state-of-the-art coupled land-atmosphere models that allows simulations at both convection-parameterized and convection-permitting resolution. It is an observation-driven modeling system that integrates aerosol, cloud, precipitation, and land processes at spatial resolutions of 1 – 25 km (Peters-Lidard et al., 2015). The NU-WRF model combines the National Center for Atmospheric Research (NCAR) Advanced Research WRF (ARW) (Skamarock et al., 2008) dynamical core atmospheric model with the Goddard Space Flight Center (GSFC) Land Information System (LIS) (Kumar et al., 2006, 2008) for the land component. LIS integrates the use of high-resolution satellite data, advanced land surface models (LSMs), and high-performance computing tools at high resolution. The LIS framework has multiple LSMs, one of which is the Noah-MP LSM (Niu et al., 2011). Table 1 summarizes the most important configuration options used in this study and the input datasets along with their original resolution.

**Table 1.** Overview of key model configuration and spatial input datasets.

Component	G4ICE - 9 km	G4ICE - 3 km	THOM - 9 km	THOM - 3 km
Land surface model		Noah-MP version 3.6		
Surface layer drag coefficient		Chen97		
Land use		MODIS including lake category (1 km)		
Topography	Global Multi-resolution Terrain Elevation Data 2010 (30 arcsec)			
Surface albedo		NCEP_Native (0.144°)		
Greenness fraction		NCEP_Native (0.144°)		
Microphysics	Goddard 4ICE	Goddard 4ICE	Thompson	Thompson
Planetary boundary layer		Mellor-Yamada-Janjic		
Cumulus parameterization	Grell-Dévényi	N/A	Grell-Dévényi	N/A
Longwave and shortwave radiation		Goddard 2017 radiation scheme		
Meteorological forcing		MERRA-2 (0.625°x0.5°)		

### 136 2.2.1 Land Surface

137 In this study, the Noah-MP version 3.6 is used as the LSM. This model has improved  
138 land physics compared to the standard Noah LSM, i.e. with advancements in the physics  
139 for surface fluxes, skin temperature, and runoff (Niu et al., 2011). The complete config-  
140 uration settings can be found in the configuration file that is provided in the open data  
141 repository (see 'Open Research' section). The used settings are the default for Noah-MP,  
142 as outlined in the source code, with the exception of the surface layer drag coefficient.  
143 Various studies demonstrated the high sensitivity of surface energy fluxes to the choice  
144 of surface layer drag coefficient, with region-specific performance differences (e.g. Niu  
145 et al. (2011); Yang et al. (2011)). Tests with the default setup including the Monin-Obukhov  
146 similarity scheme (Brutsaert, 1982) resulted in a strong underestimation of simulated light-  
147 ning occurrence for all indices. Tests with the Chen97 scheme (Chen et al., 1997) resulted  
148 in a more realistic number of lightning occurrences for both convection-parameterized.  
149 As indicated by Yang et al. (2011), the surface layer drag coefficient is the most impor-  
150 tant factor for modeling land skin temperature. Therefore, one can conclude that with  
151 the given model setup, the Chen97 scheme results in a better representation of the land  
152 skin temperature, and consequently surface energy fluxes. Given the importance of sur-  
153 face energy fluxes for deep convection, Chen97 was subsequently used for all simulations.

154 Because the default NU-WRF sea surface temperature (SST) data input derived  
155 from microwave and infrared sensors (Wentz et al., 2016) was found to not be reliable  
156 for the Great Slave Lake in our study area, we used SST data input from the Group for  
157 High Resolution SST (GHRSST) level 4 SST daily analysis (Hoyer et al., 2014; Danish  
158 Meteorological Institute, Center for Ocean and Ice, 2007). This SST data is then used  
159 for those grid cells that are identified as lakes by the land use classification (Table 1) to  
160 calculate surface energy fluxes (NASA, 2020).

### 161 2.2.2 Atmosphere

162 The choices for the atmospheric MP, planetary boundary layer (PBL), and cumu-  
163 lus parameterization scheme are based on 13 papers on the use of WRF or NU-WRF to  
164 model convection (Blake et al., 2017; Fierro et al., 2013; Gharaylou et al., 2020; Iguchi  
165 et al., 2017; Madala et al., 2014; Santanello et al., 2013; W. K. Tao et al., 2016; Z. Tao  
166 et al., 2020; Wong et al., 2013; Lang et al., 2014; Comin et al., 2018; Dawn & Satyanarayana,  
167 2020; Gilliland & Rowe, 2007). The literature study indicated that the highest sensitiv-  
168 ity and uncertainty of the atmospheric simulations was related to the choice of the MP

169 scheme. To address this issue, two MP schemes, the Goddard 4ICE (W. K. Tao et al.,  
 170 2014) and Thompson (Thompson et al., 2008) MP schemes, are used and compared in  
 171 this study. These two schemes are among the most commonly used MP schemes and are  
 172 both proven to be able to represent the atmospheric processes, such as deep convection,  
 173 in both temperate and arctic regions (Lang et al., 2014; He & Loboda, 2020). Since the  
 174 boreal region is geographically and climatologically located between these two regions,  
 175 we decided that these two MP schemes are likely to best represent the atmospheric pro-  
 176 cesses in the boreal zone. To our knowledge, no literature on the boreal region compar-  
 177 ing different MP schemes exists. In terms of PBL and cumulus parameterization, liter-  
 178 ature did show one clear superior option in combination with the selected MP schemes.  
 179 Both MP schemes proved to perform especially well in combination with the Mellor-Yamada-  
 180 Janjic PBL scheme (Mellor & Yamada, 1982). This scheme outperforms other PBL schemes  
 181 in the representation of thunderstorms (Madala et al., 2014). For the convection param-  
 182 eterization of WRF9 (9 km), the Grell-Dévényi cumulus ensemble (Grell & Dévényi, 2002)  
 183 is used.

184 The use of two different MP schemes for two spatial model resolutions results in  
 185 four different model configurations: (i) the Goddard 4ICE MP scheme at 9 km (G4ICE -  
 186 9 km), (ii) the Goddard 4ICE MP scheme at 3 km (G4ICE - 3 km), (iii) the Thompson  
 187 MP scheme at 9 km (THOM - 9 km), and (iv) the Thompson MP scheme at 3 km spa-  
 188 tial resolution (THOM - 3 km). Lightning occurrences are diagnosed from each of these  
 189 four model configurations using four different lightning indices, resulting in 16 numer-  
 190 ical experiments.

## 191 2.3 Lightning Indices

192 Some lightning indices can be used to determine lightning flash densities directly,  
 193 whereas others provide a lightning probability that then needs to be converted into light-  
 194 ning flash densities. Several lightning indices exist with various levels of complexity, span-  
 195 ning from the approach of Price and Rind (1992), based on the convective cloud top height,  
 196 to those approaches based on the evolving electric field in storms, such as the lightning  
 197 index of Fierro et al. (2013).

198 In this study, four different lightning indices are compared: (i) the Lightning Po-  
 199 tential Index (LPI) of Yair et al. (2010), (ii) the lightning threat (LT) of McCaul et al.  
 200 (2009), (iii) the Price and Rind (1992) index based on maximal updraft velocity (PR92W),  
 201 and (iv) the product of CAPE and convective precipitation rate (CAPEXP) developed  
 202 by Romps et al. (2014). All indices are diagnosed from the hourly NU-WRF output.

### 203 2.3.1 LPI

204 The LPI ( $\text{J kg}^{-1}$ ) is an empirical index that is based on ice fractions and super-  
 205 cooled liquid water mixing ratios in the region between 0 and  $-20^\circ\text{C}$ . In this tempera-  
 206 ture range, the noninductive mechanisms that involve the collision of ice and graupel par-  
 207 ticles are most effective, because they require the presence of super-cooled liquid water  
 208 to have charge separation due to the rebounding collisions between graupel and cloud  
 209 ice crystals (Saunders, 2008). This index does not directly estimate the flash density but  
 210 is a measure of the potential for charge generation and separation that leads to light-  
 211 ning (Yair et al., 2010; Lynn & Yair, 2010). It is calculated from the vertical updraft ve-  
 212 locity and the mixing ratios of liquid water, cloud ice, snow, and graupel.

$$LPI = 1/V \int \int \int \epsilon w^2 dx dy dz \quad (1)$$

213 where  $V$  is the volume of air in the layer between 0 and  $-20^\circ\text{C}$ ;  $w$  is the vertical up-  
 214 draft velocity ( $\text{m s}^{-1}$ );  $dx$  and  $dy$  are the horizontal, and  $dz$  the vertical dimensions of  
 215 the grid cell (m); and  $\epsilon$  is a dimensionless number between 0 and 1:

$$\epsilon = \frac{2(Q_i Q_l)^{0.5}}{(Q_i + Q_l)} \quad (2)$$

216 where  $Q_l$  is the total liquid water mass mixing ratio ( $\text{kg kg}^{-1}$ ); and  $Q_i$  is the ice  
217 fractional mass mixing ratio ( $\text{kg kg}^{-1}$ ), which is defined as:

$$Q_i = q_g \left[ \left( \frac{(q_s q_g)^{0.5}}{(q_s + q_g)} \right) + \left( \frac{(q_i q_g)^{0.5}}{(q_i + q_g)} \right) \right] \quad (3)$$

218 where  $q_i$ ,  $q_g$ , and  $q_s$  are the mass mixing ratios for cloud ice, graupel, and snow,  
219 respectively (all in  $\text{kg kg}^{-1}$ ).

### 220 **2.3.2 McCaul Lightning Threat**

221 The McCaul Lightning Threat (LT) ( $\text{flashes (5min} \cdot \text{gridbox)}^{-1}$ ) is a linear com-  
222 bination of (i) the upward fluxes of precipitating ice hydrometeors in the mixed-phase  
223 region at the  $-15^\circ\text{C}$  level and (ii) the vertical integral of cloud ice, graupel and snow, as  
224 follows:

$$LT = 0.95k_1(wq_g)_m + 0.05k_2 \int \rho(q_g + q_s + q_i)dz \quad (4)$$

225 where  $k_1 = 0.042$ ;  $k_2 = 0.20$ ;  $w$  is the vertical updraft velocity ( $\text{m s}^{-1}$ );  $\rho$  is the  
226 air density ( $\text{kg m}^{-3}$ ); and  $q_i$ ,  $q_g$ , and  $q_s$  are the cloud ice, graupel and snow mixing ratio,  
227 respectively. The subscript  $m$  indicates the  $-15^\circ\text{C}$  level.

### 228 **2.3.3 PR92W**

229 The PR92W index ( $\text{flashes (min)}^{-1}$ ) is based on the relation between maximum  
230 updraft velocity ( $w_{max}$ ; in  $\text{m s}^{-1}$ ) and the number of flashes per minute:

$$PR92W = c \cdot 5 \cdot 10^{-6} w_{max}^{4.54} \quad (5)$$

231 where  $c$  is a calibration factor used to generalize the original equation from a 5 km spa-  
232 tial resolution to all possible resolutions (Price & Rind, 1994). The calibration factor  $c$   
233 is defined as:

$$c = 0.97241 e^{0.048203R} \quad (6)$$

234 where  $R$  is the grid cell area in squared degrees. Price and Rind (1994) state that this  
235 calibration factor does not depend on the latitude or longitude. These relatively simple  
236 relations have been shown to perform relatively well at different spatial resolutions (rang-  
237 ing from 1 - 36 km) by several studies (Ushio et al., 2001; Yoshida et al., 2009; Barthe  
238 et al., 2010; Wong et al., 2013) and were for a long time the most frequently used light-  
239 ning indices.

### 240 **2.3.4 CAPE $\times$ P**

241 The last lightning index used in this study is the product of convective available  
242 potential energy (CAPE, in  $\text{J kg}^{-1}$ ) and the convective precipitation rate (P, in  $\text{kg (m}^2\text{s)}^{-1}$ ),  
243 expressed in flashes ( $\text{m}^2\text{s)}^{-1}$ , as developed by Romps et al. (2014). This product is a good  
244 proxy for lightning distribution over land when multiplied with a constant of proportion-  
245 ality ( $\eta/E$ ) to convert it to a flash density:

$$\text{CAPE} \times \text{P} = \eta/E \cdot \text{CAPE} \cdot \text{P} \quad (7)$$

where  $\eta/E$  consists of the dimensionless conversion efficiency  $\eta$  and the energy discharge per flash  $E$  (in J). Romps et al. (2014) found that CAPEXP correlates best with the observed lightning with  $\eta/E$  equal to  $1.3 \cdot 10^{-11} \text{J}^{-1}$  (Romps et al., 2014).

Since the NU-WRF model only simulates convective precipitation rate when a convective parameterization scheme is used (only activated for 9 km simulations), the convective precipitation rate used for the CAPEXP index in this study is determined based on the method described in Churchill and Houze (1984). They defined convective cores as grid cells with twice the rainfall rate of the background (2 grid cells in each direction) average or any grid cell with a rain rate of  $>20 \text{ mm h}^{-1}$ . The grid cells directly surrounding the convective center are also considered convective regions. To keep the results of the two resolutions comparable, this method was used to determine convective precipitation for both the 3 and 9 km simulations.

## 2.4 Evaluation

### 2.4.1 Lightning Observations

The observational data used for evaluation is provided by the Canadian Lightning Detection Network (CLDN). The data covers the area between  $58 - 66^\circ\text{N}$  and  $108 - 125^\circ\text{W}$  for the years 2015 – 2020. Earlier data are available but subject to large biases due to the use of older sensor technology and therefore not used. The dataset consists of individual flashes measured with a spatial and temporal precision of  $0.0001^\circ$  (approximately 5 m) and  $10^{-3}$  s, respectively. A classification into cloud-cloud and cloud-ground lightning is also provided.

For further evaluation, the observational data is converted to an hourly flash density at the two different resolutions. The flashes are summed regardless of the type (cloud-cloud or cloud-ground) since the different lightning indices used in this study do not differentiate between types of flashes.

### 2.4.2 Rescaling of Lightning Indices

The lightning indices derived from all experiments are rescaled to the observations. This is on the one hand needed to convert the LPI, which represents the potential for lightning to occur, to a flash density and on the other hand to allow a consistent comparison across lightning indices. We followed the two-step procedure as described in Brisson et al. (2021). First, the excessive small flash densities are eliminated so that the total sum (in both space and time) of modeled lightning flashes equals the total sum of observed lightning flashes. In a second step, a linear function is derived to relate the model output to the observed flash densities. Note that each lightning index is rescaled by a single linear model for the entire domain which makes overfitting issues very unlikely given the large sample size. Note that the approach is applicable to climate change scenarios since the same linear equation could be used to rescale future predictions without altering the climate change signal as demonstrated in Brisson et al. (2021).

### 2.4.3 Evaluation: Precipitation and Surface Energy Fluxes

The ability of the model to accurately simulate surface energy fluxes is key to the quality of lightning predictions. Therefore, the modeled LH and SH as well as total precipitation patterns of the different model configurations are evaluated in a first step. This is done by comparing the spatial patterns of the 6-year summer averages of the precipitation, LH, and SH modeled by the different model configurations against MERRA-2 re-analysis data.

291

#### 2.4.4 Evaluation: Spatiotemporal Frequency Distribution of Lightning

292

293

294

295

296

To evaluate the frequency distribution of the modeled lightning indices to that of the observations, the spatiotemporal probability density functions (PDF; not shown) are calculated for each index. The PDFs are then compared to the observations using the Perkins skill score (PSS) (Perkins et al., 2007) from a rescaled flash density of  $0.1 \text{ flashes (h km}^2\text{)}^{-1}$  onward. The PSS measures the common area between two PDFs as follows:

$$\text{PSS} = \sum_{i=1}^n \min(z_s(i), z_o(i)) \quad (8)$$

297

298

299

300

301

where  $i$  is the bin index;  $n$  is the total number of bins; and  $z_o(i)$  and  $z_s(i)$  are the relative frequencies of a given bin from the observations and model, respectively. The PSS is a measure for non-linearities between two datasets. A PSS of 1 means that two PDFs are identical, while a value  $< 0.7$  indicates that the two PDFs differ significantly according to Perkins et al. (2007).

302

#### 2.4.5 Evaluation: Spatial Pattern and Diurnal Climatology of Lightning

303

304

305

306

307

308

309

To evaluate the different experiments in terms of their capability to simulate lightning in space and time, the 6-year average spatial patterns of daily flash densities and the 6-year averaged diurnal cycle are computed. The results are compared with the CLDN observations by means of the spatial Pearson correlation coefficients (R), for each of the experiments. For the diurnal cycle, the 6-year averaged diurnal cycle is for each grid cell in space evaluated against the CLDN observations. For consistency, the results of the 3 km experiments are regridded to match the resolution of the 9 km simulations.

310

#### 2.4.6 Evaluation: Event-Based Skill Assessment of Lightning

311

312

313

314

315

316

317

318

319

320

321

322

Lastly, the predictive performance of the different experiments is also evaluated on an 'event-by-event' (i.e. grid cell per grid cell and time step per time step) basis by using the following evaluation metrics: (i) the probability of detection (POD, equation 9), (ii) the critical success index (CSI, equation 10), (iii) the bias (equation 11), and (iv) the success ratio (SR, equation 12). These four metrics can be easily presented together in a single "performance diagram" as shown in Roebber (2009). The POD, CSI and SR all range between 0 and 1, with 1 a perfect score. The bias, defined here as the ratio of the observed events and the predicted events, ranges from 0 to infinity, but still has 1 as a perfect score. Because of the way Roebber (2009) designed their performance diagram, predictions that are further to the top-right are more accurate than points closer to the bottom-left. Additionally, ideal predictions are located on the bias=1 diagonal. The metrics are calculated as follows,

$$\text{POD} = \frac{\text{TP}}{\text{TP} + \text{FN}} \quad (9)$$

$$\text{CSI} = \frac{\text{TP}}{\text{TP} + \text{FP} + \text{FN}} \quad (10)$$

$$\text{bias} = \frac{\text{TP} + \text{FP}}{\text{TP} + \text{FN}} \quad (11)$$

$$\text{SR} = 1 - \frac{\text{FP}}{\text{TP} + \text{FP}} \quad (12)$$

323

324

where TP, FP, TN, and FN are the true positive (hits), false positive (false alarms), true negative (correct negatives), and false negative (misses) lightning predictions.

325

326

To calculate these four skill metrics, the model output and the observations are aggregated to a  $72 \times 72 \text{ km}^2$  grid and a 6-hourly time interval. This aggregation was done

327 to reduce the effects of the temporal and spatial inaccuracy of the atmospheric inputs  
 328 on the skill of the lightning indices. The performance diagram proposed by Roebber (2009)  
 329 provides a summary of both spatial and temporal simulation performance.

### 3 Results and Discussion

330

331

#### 3.1 Precipitation and Surface Energy Fluxes

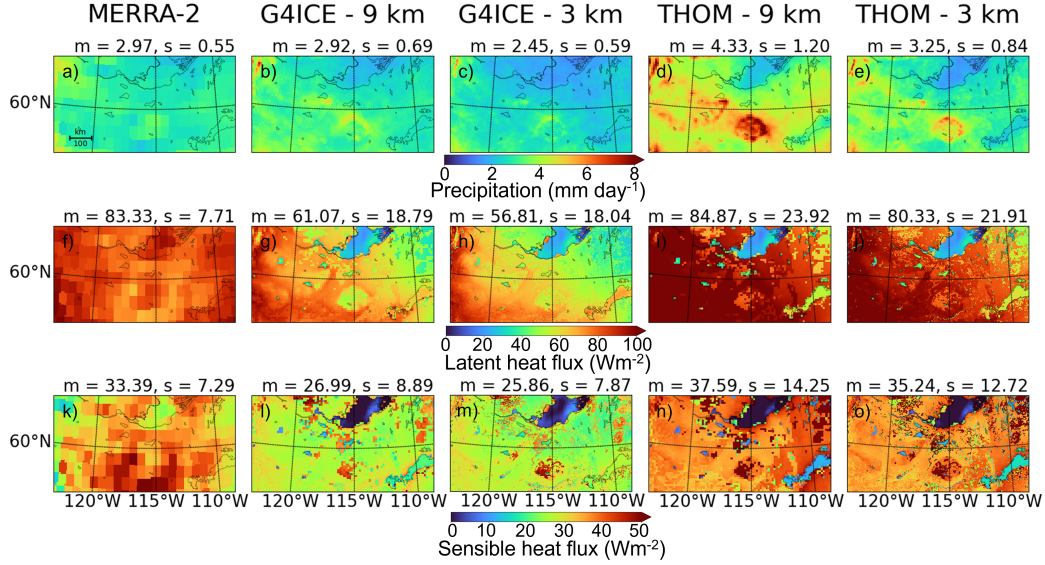


**Figure 2.** 6-year averaged summer precipitation (a-e), latent heat flux (f-j) and sensible heat flux (k-o) estimated by MERRA-2 and the 4 different model configurations (G4ICE - 9 km, G4ICE - 3 km, THOM - 9 km and THOM - 3 km). The spatial mean (m) and standard deviation (s) are provided at the top of each figure.

332

333

334

335

336

337

Figure 2 shows the 6-year (2015-2020) averaged daily precipitation, LH, and SH from the NU-WRF simulations compared with MERRA-2 data. MERRA-2 (first column) has a known yearly average positive bias for the boreal summer LH of  $20 \text{ W m}^{-2}$  and globally overestimates the SH by  $6 \text{ W m}^{-2}$ , on average (Draper et al., 2018). Although these biases were not determined specifically for our study domain, they here serve as indication of a possible bias.

338

339

340

341

342

343

344

345

346

347

348

349

350

351

Compared to the MERRA-2 data, the G4ICE - 9 km simulation shows a similar mean precipitation (2.92 and  $2.97 \text{ mm day}^{-1}$  for G4ICE - 9 km and MERRA-2, respectively), whereas the G4ICE - 3 km simulation shows a slight underestimation ( $2.45 \text{ mm day}^{-1}$ ). Both the THOM - 9 km and THOM - 3 km simulations show an overestimation of the spatially averaged daily precipitation rate, with  $4.33$  and  $3.25 \text{ mm day}^{-1}$ , respectively. The THOM simulations mainly show a higher precipitation rate around topographic structures in the center and western part of the study domain (see Figure 1b), likely associated with orographic precipitation (Smith, 1979). This sensibility to topography is also seen for the G4ICE simulations and MERRA-2 but is less pronounced. Orographic clouds are primarily composed of supercooled liquid water. Therefore, the representation of this microphysical variable by the MP scheme will greatly influence the presence of orographic precipitation (Sarmadi et al., 2019). Since the G4ICE MP is a single moment scheme and the THOM MP is a double moment scheme, both schemes simulate hydrometeors differently (Dawn & Satyanarayana, 2020). Sarmadi et al. (2019) also found that differ-

ences in simulated precipitation are mainly due to uncertainties in the physical processes of the model. Thus, the difference in simulated hydrometeors explains part of the observed differences in precipitation.

Both MP schemes produce a southwest-northeast gradient of decreasing LH, while for SH, the gradients disagree. The G4ICE simulations show a southwest-northeast gradient of decreasing SH, while the opposite is observed for the THOM simulations. For both surface energy fluxes, MERRA-2 shows a more uniform pattern of generally higher values. The differences are strongest over the Great Slave Lake where both MP schemes produce lower surface energy fluxes. Despite their diverging spatial gradients, the spatial means of the LH of both THOM simulations (84.87 and 80.33  $\text{W m}^{-2}$  for 9 km and 3 km resolution, respectively) are similar to that of the MERRA-2 (83.33  $\text{W m}^{-2}$ ), while those of the G4ICE simulations are significantly lower (61.07 and 56.81  $\text{W m}^{-2}$ , respectively). Similar conclusions can be made for the average SH, with the G4ICE simulations showing lower averages compared to both MERRA-2 and the THOM simulations. The fact that both LH and SH are lower for G4ICE, indicates that this MP scheme reflects more radiation than the THOM scheme. This consequently results in lower surface temperatures (not shown here).

### 3.2 Lightning Simulations

#### 3.2.1 Spatiotemporal Frequency Distribution

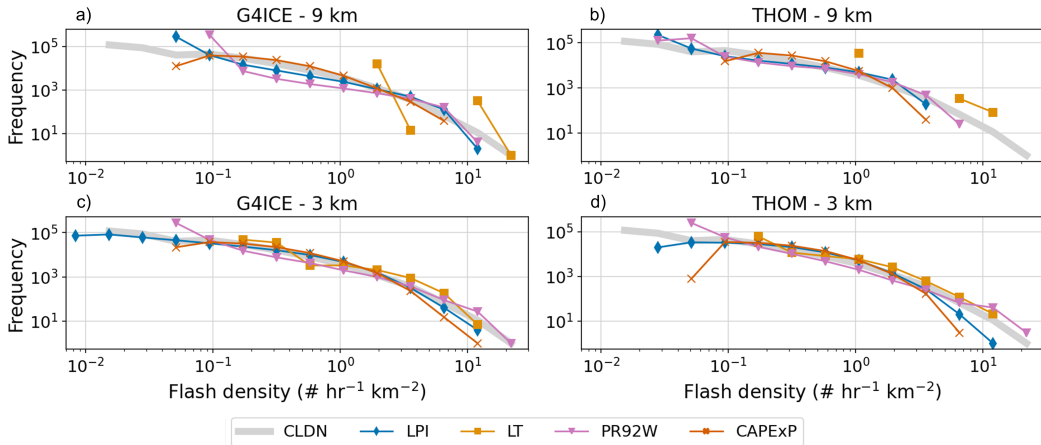


**Figure 3.** Spatiotemporal frequency distributions of the domain average hourly flash rates for each model configuration as observed (gray), as represented by the LPI, LT3, PR92W, and CAPEXP parameterizations after linear rescaling to match the observations.

Figure 3 compares the spatiotemporal frequency distribution of the observed hourly flash density (in gray) and the model output for each experiment. The PSS values of these frequency distributions are presented in Table 2. The time dependent graphs in Figure 3 and the tabular data of PSS in Table 2 together show a clear improvement at 3 km compared to 9 km for all experiments, with the exception of PR92W for the THOM MP (PSS of 0.88 and 0.87 for 9 and 3 km, respectively), and CAPEXP for the G4ICE MP (with a PSS value of 0.94 for both resolutions). The largest improvements can be seen for the LT index, with PSS values increasing from 0.02 to 0.65 and from 0.08 to 0.78 for the G4ICE and THOM simulations, respectively. Note that the PSS is only calculated for flash densities higher than 0.1 flashes  $\text{h}^{-1} \text{km}^{-2}$ , as the lower values were influenced by the cutoff value applied during the rescaling (see section 2.4.2).

382 Both MP schemes fail to provide an accurate prediction for LT, with only three or  
 383 four different predicted flash densities at 9 km. For the other indices, the G4ICE - 3 km  
 384 model configuration provides the highest PSS values. This model configuration also cap-  
 385 tures both the lowest as the highest flash densities better than the other configurations,  
 386 as shown in Figure 3. This superiority of the convection-permitting resolution can also  
 387 be seen for the THOM MP scheme.

**Table 2.** PSS values for the different model configurations and indices.

Index	G4ICE - 9 km	G4ICE - 3 km	THOM - 9 km	THOM - 3 km
LPI	0.89	0.93	0.89	0.91
LT	0.02	0.65	0.08	0.78
PR92W	0.81	0.88	0.88	0.87
CAPE <sub>ExP</sub>	0.94	0.94	0.90	0.91

### 388 3.2.2 Spatial Patterns

389 The spatial pattern of the 6-year average flash density of the CLDN observations  
 390 (Figure 4a-d) shows a southwest-northeast gradient of decreasing lightning. The main  
 391 cluster of lightning for the CLDN observations also shows agreement with the greenness  
 392 fraction shown in Figure 1. This cluster is not seen in the simulation output. For the  
 393 G4ICE simulations, the main area of lightning is in the southern half of the study do-  
 394 main, with relatively few flashes in the northeastern corner. The main cluster for the THOM  
 395 simulations has shifted towards the center of the domain, especially for LPI and CAP-  
 396 ExP. A comparison of the spatial R values shown in Figure 5 shows that the G4ICE -  
 397 3 km configuration ( $R = 0.43 - 0.57$ ), is superior to the other model configurations in  
 398 terms of predicting the spatial pattern of the CLDN observations, with the exception of  
 399 the CAPE<sub>ExP</sub> index, which performs better at a coarser resolution. Even though this model  
 400 configuration also fails to predict the exact cluster of the observed lightning occurrences,  
 401 it does show the southwest-northeast gradient of decreasing lightning that is also in the  
 402 CLDN observations. THOM - 3 km also shows higher correlations than THOM - 9 km,  
 403 except for CAPE<sub>ExP</sub> ( $R = 0.26$  and  $0.25$  at 9 km and 3 km, respectively). Romps et al.  
 404 (2018) found that CAPE<sub>ExP</sub> performed very well at a  $0.5^\circ$  grid, indicating that this in-  
 405 dex might work better at a coarser resolution. Brisson et al. (2021) state that CAPE<sub>ExP</sub>  
 406 shows problems at convection-permitting resolutions because explicitly resolving con-  
 407 vection leads to a null CAPE if there is convective precipitation. Prein et al. (2015), on  
 408 the other hand, found that convection-permitting resolutions improved the representa-  
 409 tion of extreme precipitation and summertime convection. Both are directly used by the  
 410 CAPE<sub>ExP</sub> index. This better representation of convection at the finer resolution also ex-  
 411 plains the better performance of the indices that depend on the maximum vertical up-  
 412 draft velocity, as convection determines the theoretical maximum updraft velocity (Bao  
 413 & Sherwood, 2019).

414 For all four model configurations, LT and PR92W show clear line structures that  
 415 are not seen for any of the other indices. Both indices depend strongly on the maximal  
 416 vertical updraft velocity (see equations 4 and 5). Among all other indices, only LPI is  
 417 dependent on the updraft velocity, but also strongly depends on other atmospheric vari-  
 418 ables (see equation 1). A map of the maximal updraft velocity for each grid cell (not shown  
 419 here) shows very similar line-like structures as those seen for LT and PR92W, support-  
 420 ing this strong dependence on this atmospheric variable. One weather phenomenon that  
 421 is known to go along strong updrafts is a squall line, a line of thunderstorms that forms  
 422 along a cold front and is characterized by frequent lightning and strong updrafts (Newton,  
 423 1950). Another explanation is so-called topographic convergence. The observed line struc-

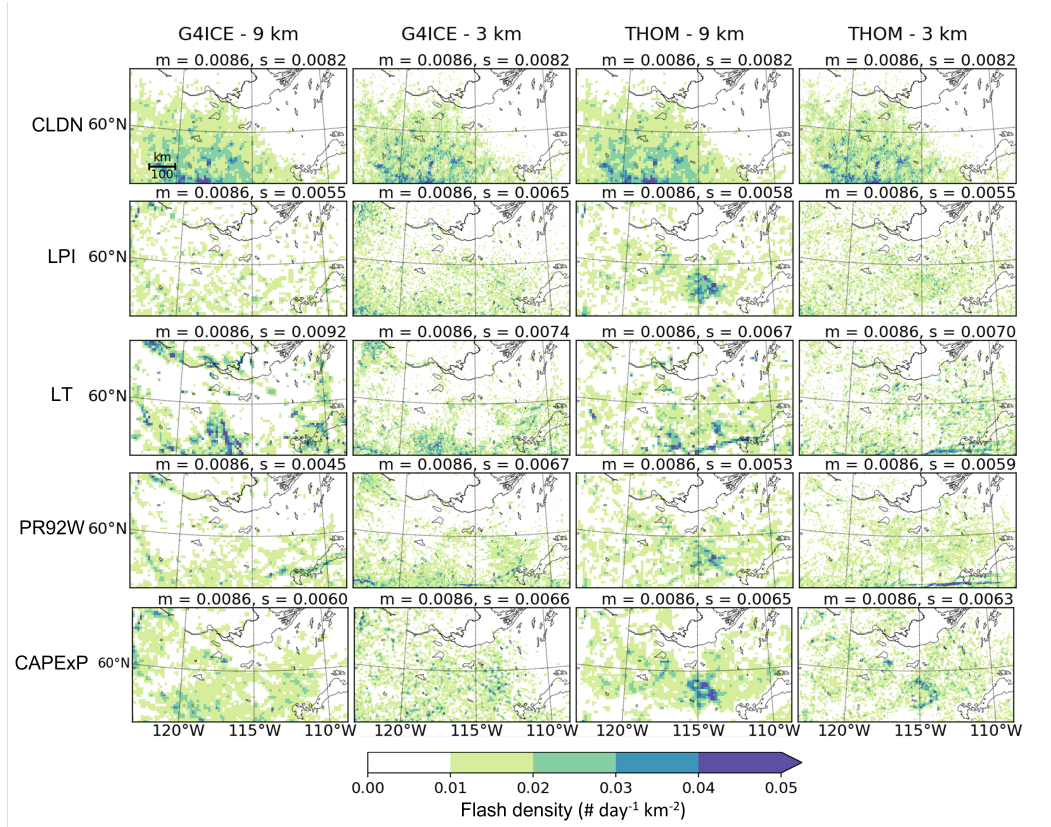


**Figure 4.** 6-year average total daily flash density for the months of June through August of 2015-2020 for the observations (CLDN), LPI, LT, PR92W, and CAPEXP parameterizations and for each model configuration (G4ICE - 9 km, G4ICE - 3 km, THOM - 9 km and THOM - 3 km). The spatial mean (m) and standard deviation (s) are provided at the top of each figure.

424 tures correlate well with the location of terrain height differences, as shown in Figure 1.  
 425 Due to the elevated terrain, the wind flow is forced to go up and around the topographic  
 426 structure, which can cause convective uplift near complex topography (Barthlott et al.,  
 427 2006).

428 The CAPEXP index shows a very low flash density of  $< 0.01$  flashes  $\text{h}^{-1} \text{km}^{-2}$  for  
 429 the THOM simulations over and around Lake Athabasca in the southeast, making it stand  
 430 out from the surroundings. While this is also true for the G4ICE model configurations  
 431 over the lake, these experiments do show lightning at the edge of the lake. This can be  
 432 explained by the difference in relative LH and SH over this lake compared to the sur-  
 433 rounding land for both MP schemes (Figure 2). For the THOM experiments, both LH  
 434 and SH over this lake are smaller than for the surrounding land. This implies that there  
 435 is less energy for the formation of strong thunderstorms over the lake as compared to the  
 436 land (Beringer & Tapper, 2002). For the G4ICE simulations, the LH of the lake is higher  
 437 than that of the surrounding land and SH is only slightly smaller. In absolute values,  
 438 the fluxes over the lake are higher for the G4ICE than for the THOM experiments. Since  
 439 CAPE is highest when both LH and SH are high, this all leads to more predicted thun-  
 440 derstorms around Lake Athabasca for the G4ICE simulations.

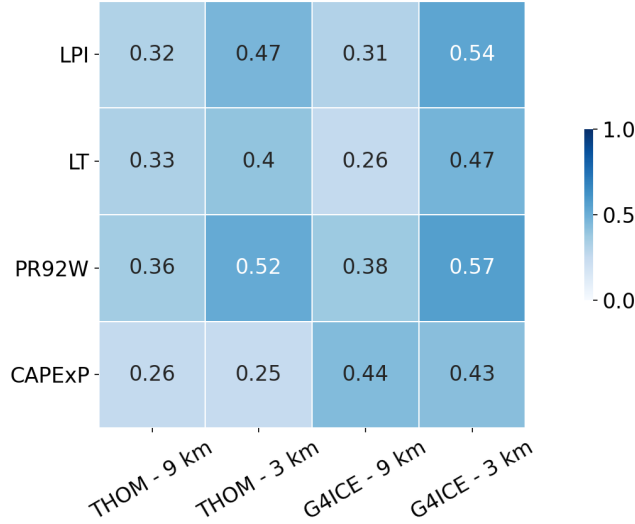


**Figure 5.** Spatial Pearson correlation coefficients between the 6-year summer average of each lightning index and the CLDN observations for the 4 model configurations.

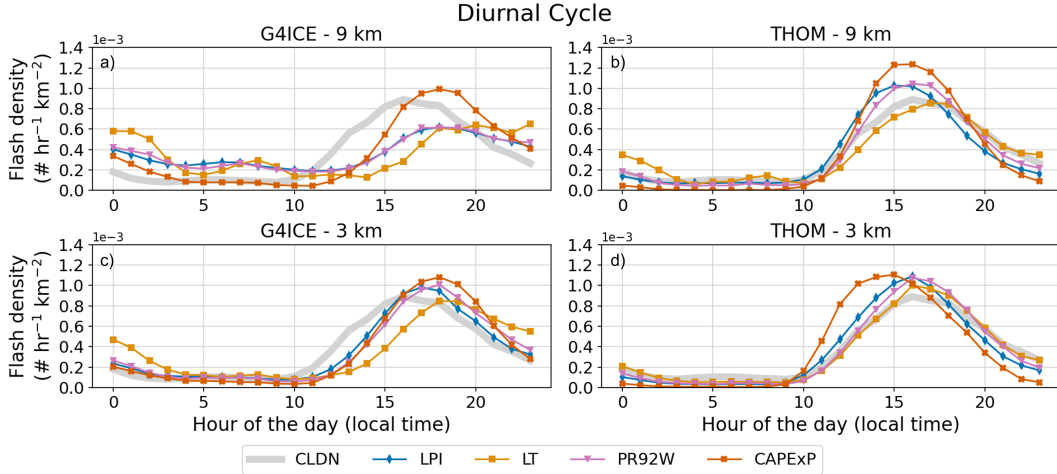


**Figure 6.** Six-year average diurnal cycle of the domain average flash density for each experiment, diagnosed by the LPI, LT, PR92W, CAPEXP indices, and compared to (gray) observations.

441

### 3.2.3 Diurnal Climatology

442

443

444

445

446

447

Figure 6 shows the diurnal cycles of the lightning indices for each experiment together with that of the CLDN observations (in gray). All diurnal cycles exhibit a peak in the afternoon around 3-5 pm local time, which matches with the peak in the reference observations. Both THOM experiments better predict the diurnal cycle than the G4ICE experiments, especially at the coarser resolution and early in the morning. This better performance is also shown by the higher temporal R values (see Figure 7).

448

449

450

The diurnal cycles of the THOM simulations show a very clear peak in the afternoon, starting 1 or 2 hours before (for CAPEXP and LPI of THOM - 3 km) to 1 hour after (for LT of THOM - 9 km) the observed peak. The G4ICE simulations, on the other

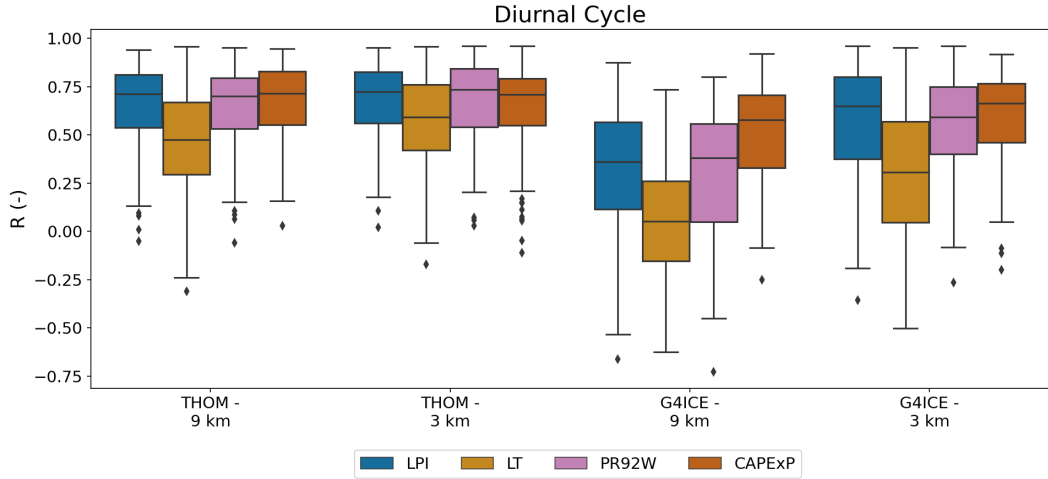


**Figure 7.** Temporal Pearson correlation coefficients ( $R$ ) between simulated and observed (CLDN) six-year averaged diurnal cycle of flash density calculated for each grid cell, and grouped by lightning index and experiment.

451 hand, generally peak one to three hours after the observed peak. These differences be-  
 452 tween the simulated and observed peak are reduced for the 3 km simulations, with the  
 453 exception of CAPEXP for the THOM - 3 km experiment, for which the peak is now shifted  
 454 to approximately 2 hours before the observed peak. In terms of absolute values, the CAP-  
 455 ExP index for the THOM - 9 km experiment greatly overestimates the observed peak,  
 456 whereas for the G4ICE - 9 km experiment, all indices, except CAPEXP, underestimate  
 457 the peak. The diurnal cycles in Figure 6 and the Pearson correlation coefficients in Figure  
 458 7 show the best agreement between CAPEXP and the observed diurnal cycle, confir-  
 459 ming the findings of Romps et al. (2018) that CAPEXP is good at capturing the tim-  
 460 ing of the observed diurnal cycle. However, for the THOM - 3 km simulations, the LPI  
 461 performs better. For all experiments, LT is the least capable of capturing the diurnal cy-  
 462 cle of the observations.

463 **3.2.4 Overall Event-Based Skill Assessment**

464 In the previous sections, the performance of the different experiments and light-  
 465 ning indices was evaluated either for a strong aggregation in space (long-term spatial pat-  
 466 tern) or in time (diurnal cycle, frequency distribution), and on the basis of flash densi-  
 467 ties. Here we present an additional assessment on an event-by-event basis using the pre-  
 468 dictive skill scores (POD, CSI, SR, and bias) that do not take into account the absolute  
 469 flash densities but only the presence or absence of lightning. It is important to note that  
 470 the bias used here is not following the conventional definition of bias in statistics, i.e. it  
 471 is not the difference between the predictions and the observations, but rather the ratio  
 472 of total (in both space and time) predicted grid cells with lightning occurrence over the  
 473 total observed grid cells with lightning. By this definition, the bias does not take the tem-  
 474 poral and/or spatial mismatch between the model and observations into account. This  
 475 mismatch is represented in the POD, CSI, and SR.

476 Figure 8 represents the performance diagram as described in Roebber (2009), show-  
 477 ing the POD versus the SR. The blue contours represent the CSI and dashed lines the  
 478 bias. Points further to the top right indicate a better overall accuracy for that exper-  
 479 iment. Figure 8 shows that, by comparing for each index the different model configura-  
 480 tions, the 3 km simulations (green) systematically have a higher POD, SR, and CSI. The

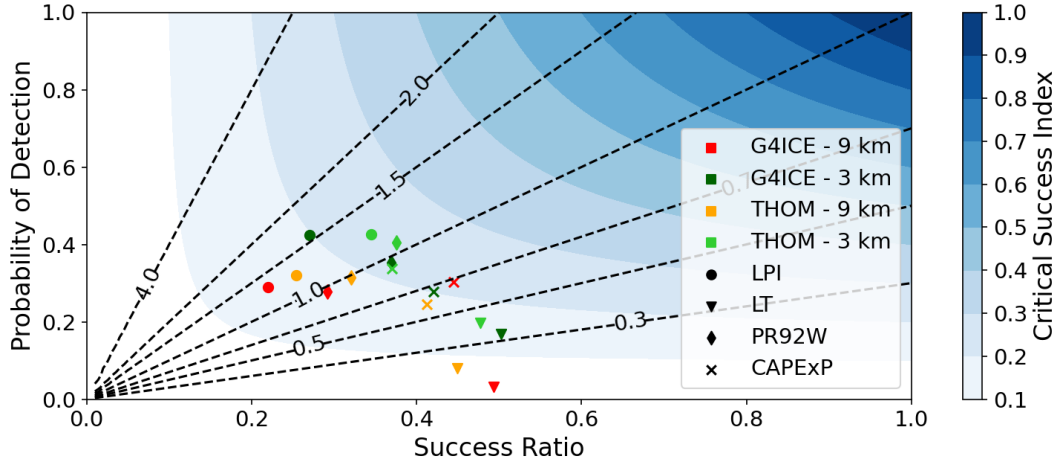


**Figure 8.** Performance diagram of the POD on the y-axis versus SR on the x-axis. The blue contours represent the CSI and the dashed lines represent the bias. The skills were calculated on a  $72 \times 72 \text{ km}^2$  grid and aggregated over six hours. Different colors indicate different experiments, while different markers indicate the different lightning indices.

481 bias seems less influenced by the model configuration, but rather depends on the index.  
 482 This indicates that the indices a bias  $> 1$  predict a lot of lightning occurrences, whereas  
 483 those with a bias  $< 1$  predict less lightning occurrences in general, independent of the  
 484 model configuration.

485 For all four model configurations, PR92W has a bias very close to 1, indicating that  
 486 it predicts a similar amount of lightning occurrences in space and time as the observa-  
 487 tions. The LPI (only for the G4ICE - 3 km experiment) shows the highest POD, but has  
 488 a rather low SR. The LT, on the other hand, has the highest SR for all model configu-  
 489 rations, but also the lowest POD. It is noticeable that for all lightning indices, there are  
 490 clear clusters of the datapoints for the four model configurations. These clusters are some-  
 491 what expected as the natural tendency of an index to predict more/less lightning would  
 492 not change much with another MP or resolution. The different clusters can be ranked  
 493 in order of decreasing POD, bias, or increasing SR, all resulting in the same order: (i)  
 494 LPI, (ii) PR92W (bias of approximately 1), (iii) CAPEXP, and (iv) LT.

495 The high bias ( $> 1$ ) of the LPI, indicates that this index systematically predicts  
 496 more grid cells with lightning than observed after calibration. The LT, on the other hand,  
 497 has a bias  $< 1$ , indicating that it predicts less lightning occurrences than observed. By  
 498 predicting much less lightning occurrences than observed, the POD is naturally rather  
 499 low and the SR high, as there are not many mismatches if not a lot of data is available.  
 500 For the LPI, the higher POD can also be explained by the high bias: if more lightning  
 501 is predicted, the probability of detecting observed lightning is naturally higher. But this  
 502 high bias has the trade-off that there are more false alarms, and thus it has a lower SR.  
 503 PR92W and CAPEXP are in between the LPI and LT in terms of bias, POD and SR.  
 504 With the bias of the PR92W almost equal to 1 for all model configurations, and SR, POD  
 505 and CSI relatively good, especially for the 3 km simulations, this index shows a lot of  
 506 potential over this study area. The CAPEXP has more variability in terms of the skill  
 507 scores, strongly depending on the model configuration.

## 4 Conclusion

Global warming might enhance lightning activity in the boreal zone and lead to more wildfire ignitions. Therefore, there is a need for reliable lightning estimates at the different time scales of weather and climate simulations. In this paper, the NU-WRF model is evaluated with two MP schemes: (i) the Goddard 4 ICE scheme, and (ii) the Thompson scheme, both operating at a convection-parameterized (9 km) and convection-permitting (3 km) horizontal resolution, leading to four model configurations: (i) G4ICE - 9 km, (ii) G4ICE - 3 km, (iii) THOM - 9 km, and (iv) THOM - 3 km. These configurations are first compared in their capability to simulate energy fluxes throughout the domain, using MERRA-2 data as a reference. To diagnose lightning flash densities from the model output, four lightning indices (LPI, LT, PR92W, and CAPEXP) are used, resulting in 16 lightning predictions. These are evaluated for their capability to model the frequency distribution, spatial pattern and diurnal cycle of CLDN observations. Additionally, four predictive event-based skill scores are compared for all combinations of model configurations and lightning indices. The main results can be summarized as follows.

1. For the evaluation of the precipitation and the surface energy fluxes, the THOM simulations show a similar spatially averaged LH and SH as MERRA-2, which however has a known positive bias for both LH and SH. The G4ICE simulations do not show this bias and result in a spatial average of both LH and SH that is approximately 20 and 6  $\text{W m}^{-2}$  lower than those of MERRA-2.
2. For the spatial pattern, no model configuration predicts the observed cluster of high lightning occurrence in the southwestern part of the domain. Only the G4ICE - 3 km simulations are capable of reproducing the southwest-northeast gradient of decreasing lightning that is seen for the observations (with higher spatial R values than other for configurations). In general, the convection-permitting resolution is superior to the convection-parameterized resolution, except for the CAPEXP index, which is a lightning index that is known to perform better at a coarser resolution (Romps et al., 2018).
3. For the diurnal cycle, the THOM MP scheme performs better than G4ICE. CAPEXP is superior to the other lightning indices, except for the THOM - 3 km setup, and LT performs the worst. A clear benefit of using the finer resolution is only seen for the G4ICE experiments.
4. The event-based skill scores, represented in a performance diagram, support that the convection-permitting modeling at 3 km resolution leads to a generally higher performance for all model configurations and lightning indices.
5. No MP scheme is found to be superior for all evaluated aspects. Whereas the THOM MP scheme results in a better timing for most indices, the G4ICE scheme results in a better predicted spatial pattern.
6. No lightning index is found to be superior for all evaluated aspects.

Based on those results, we conclude that diagnosing lightning indices from the output of a convection-permitting model seems to be beneficial. However, we emphasize that this conclusion is only valid for the applied model configurations, that is, using another MP, PBL, or cumulus parameterization scheme might lead to a different conclusion.

Furthermore, it is important to note that the performance of all lightning indices strongly depends on the capability of the atmospheric model to accurately represent the required input parameters for the lightning indices. An error in the model representation of e.g. updraft velocity will lead to an error in the PR92W index. Our finding that no lightning index was generally superior to another is thus to be seen in light of the atmospheric model skill. The performance of the lightning indices may depend differently on forecast skill. Since the model skill of a specific forecast is not well known beforehand,

558 decisionmakers and forest managers might consider to use an ensemble of different light-  
559 ning indices for the estimation of lightning probability.

560 Based on the results from this study, we could also make some suggestions for fu-  
561 ture work. A first suggestion is based on the relative poor representation of the spatial  
562 pattern of lightning. An improved representation of the boreal land mosaic, consisting  
563 mainly of forests and peatlands, might be needed in the land surface modeling compo-  
564 nent (Bechtold et al., 2019; Qiu et al., 2018; Melton et al., 2019), since peatlands and  
565 forests substantially differ in their partitioning of energy fluxes (Helbig et al., 2020). A  
566 second suggestion, directed to future lightning predictions in different climate scenar-  
567 ios is to not use a linear rescaling to make the different lightning indices comparable. In-  
568 stead, it might be better to calibrate the different parameters of the different lightning  
569 indices in order to better account for non-linearities.

## 570 Acknowledgments

571 J. Mortelmans thanks the Research Foundation - Flanders (FWO) for funding this re-  
572 search (FWO.G095720N). The computer resources and services used in this work were  
573 provided by the High Performance Computing system of the Vlaams Supercomputer Cen-  
574 ter, funded by the Research Foundation - Flanders (FWO) and the Flemish Government.  
575 We thank Environment Canada for their generous permission to use Canadian Light-  
576 ning Data Network data as observational reference for the model output. We thank Car-  
577 los Cruz from the NU-WRF team for technical support, and Alexander Gruber and Nicole  
578 Van Lipzig for valuable feedback on the conducted research and the manuscript.

## 579 References

- 580 Adams-Selin, R. D., Van Den Heever, S. C., & Johnson, R. H. (2013). Impact of  
581 graupel parameterization schemes on idealized bow echo simulations. *Monthly*  
582 *Weather Review*, *141*(4), 1241–1262. doi: 10.1175/MWR-D-12-00064.1
- 583 Bao, J., & Sherwood, S. C. (2019). The Role of Convective Self-Aggregation in Ex-  
584 treme Instantaneous Versus Daily Precipitation. *Journal of Advances in Model-*  
585 *ing Earth Systems*, *11*(1), 19–33. doi: 10.1029/2018MS001503
- 586 Barthe, C., Deierling, W., & Barth, M. C. (2010). Estimation of total lightning from  
587 various storm parameters: A cloud-resolving model study. *Journal of Geophys-*  
588 *ical Research Atmospheres*, *115*(24), 1–17. doi: 10.1029/2010JD014405
- 589 Barthlott, C., Corsmeier, U., Meißner, C., Braun, F., & Kottmeier, C. (2006).  
590 The influence of mesoscale circulation systems on triggering convective  
591 cells over complex terrain. *Atmospheric Research*, *81*(2), 150-175. Re-  
592 trieved from [https://www.sciencedirect.com/science/article/pii/](https://www.sciencedirect.com/science/article/pii/S0169809505002577)  
593 [S0169809505002577](https://doi.org/10.1016/j.atmosres.2005.11.010) doi: <https://doi.org/10.1016/j.atmosres.2005.11.010>
- 594 Bechtold, M., De Lannoy, G. J. M., Koster, R. D., Reichle, R. H., Mahanama, S. P.,  
595 Bleuten, W., ... Tiemeyer, B. (2019). PEAT-CLSM: A Specific Treat-  
596 ment of Peatland Hydrology in the NASA Catchment Land Surface Model.  
597 *Journal of Advances in Modeling Earth Systems*, *11*(7), 2130–2162. doi:  
598 10.1029/2018MS001574
- 599 Beringer, J., & Tapper, N. (2002). Surface energy exchanges and interactions with  
600 thunderstorms during the Maritime Continent Thunderstorm Experiment  
601 (MCTEX). *Journal of Geophysical Research Atmospheres*, *107*(21), AAC  
602 3–1–AAC 3–13. doi: 10.1029/2001JD001431
- 603 Blake, B. T., Parsons, D. B., Haghi, K. R., & Castleberry, S. G. (2017). The struc-  
604 ture, evolution, and dynamics of a nocturnal convective system simulated using  
605 the WRF-ARW model. *Monthly Weather Review*, *145*(8), 3179–3201. doi:  
606 10.1175/MWR-D-16-0360.1
- 607 Bowman, D. M. J. S., Balch, J. K., Artaxo, P., Bond, W. J., Carlson, J. M.,  
608 Cochrane, M. A., ... Pyne, S. J. (2009). Fire in the earth system. *Science*,

- 609 324(5926), 481–484. doi: 10.1126/science.1163886
- 610 Brisson, E., Blahak, U., Lucas-Picher, P., Purr, C., & Ahrens, B. (2021). Con-  
 611 trasting lightning projection using the lightning potential index adapted in a  
 612 convection-permitting regional climate model. *Climate Dynamics*, 57(7-8),  
 613 2037–2051. doi: 10.1007/s00382-021-05791-z
- 614 Brisson, E., Van Weverberg, K., Demuzere, M., Devis, A., Saeed, S., Stengel, M.,  
 615 & van Lipzig, N. P. M. (2016). How well can a convection-permitting  
 616 climate model reproduce decadal statistics of precipitation, temperature  
 617 and cloud characteristics? *Climate Dynamics*, 47(9-10), 3043–3061. doi:  
 618 10.1007/s00382-016-3012-z
- 619 Brutsaert, W. (1982). *Evaporation into the Atmosphere: Theory, History, and Ap-  
 620 plications* (1st ed.). Dordrecht: Springer Netherlands. doi: 10.1007/978-94-017  
 621 -1497-6
- 622 Burrows, W. R., & Kochtubajda, B. (2010). A decade of cloud-to-ground light-  
 623 ning in canada: 1999–2008. part 1: Flash density and occurrence. *Atmosphere-  
 624 Ocean*, 48(3), 177-194. doi: 10.3137/AO1118.2010
- 625 Chen, F., Janjić, Z., & Mitchell, K. (1997). Impact of atmospheric surface-  
 626 layer parameterizations in the new land-surface scheme of the NCEP  
 627 mesoscale Eta model. *Boundary-Layer Meteorology*, 85(3), 391–421. doi:  
 628 10.1023/A:1000531001463
- 629 Churchill, D. D., & Houze, R. A. a. (1984). Development and Structure of Winter  
 630 Monsoon Cloud Clusters On 10 December 1978. *Journal of the Atmospheric  
 631 Sciences*, 41(6), 933–960. doi: 10.1175/1520-0469(1984)041(0933:dasowm)2.0  
 632 .co;2
- 633 Comin, A. N., Schumacher, V., & Justino, F. (2018). Impact of different mi-  
 634 crophysical parameterizations on extreme snowfall events in the South-  
 635 ern Andes. *Weather and Climate Extremes*, 21(January), 65–75. Re-  
 636 trieved from <https://doi.org/10.1016/j.wace.2018.07.001> doi:  
 637 10.1016/j.wace.2018.07.001
- 638 Danish Meteorological Institute, Center for Ocean and Ice. (2007). *GHRSSST  
 639 Level 4 DML\_OI Global Foundation Sea Surface Temperature Analysis  
 640 (GDS version 2)* [dataset]. NASA Physical Oceanography DAAC. doi:  
 641 <https://doi.org/10.5067/GHGDM-4FD02>
- 642 Dawn, S., & Satyanarayana, A. N. V. (2020). Sensitivity studies of cloud micro-  
 643 physical schemes of WRF-ARW model in the simulation of trailing stratiform  
 644 squall lines over the Gangetic West Bengal region. *Journal of Atmospheric  
 645 and Solar-Terrestrial Physics*, 290, 105396. doi: [https://doi.org/10.1016/  
 646 j.jastp.2020.105396](https://doi.org/10.1016/j.jastp.2020.105396)
- 647 Draper, C. S., Reichle, R. H., & Koster, R. D. (2018). Assessment of MERRA-2  
 648 land surface energy flux estimates. *Journal of Climate*, 31(2), 671–691. doi: 10  
 649 .1175/JCLI-D-17-0121.1
- 650 Fierro, A. O., Mansell, E. R., Macgorman, D. R., & Ziegler, C. L. (2013). The im-  
 651 plementation of an explicit charging and discharge lightning scheme within the  
 652 wrf-arw model: Benchmark simulations of a continental squall line, a tropical  
 653 cyclone, and a winter storm. *Monthly Weather Review*, 141(7), 2390–2415.  
 654 doi: 10.1175/MWR-D-12-00278.1
- 655 Finney, D. L., Doherty, R. M., Wild, O., Stevenson, D. S., MacKenzie, I. A., &  
 656 Blyth, A. M. (2018). A projected decrease in lightning under climate change.  
 657 *Nature Climate Change*, 8(3), 210–213. doi: 10.1038/s41558-018-0072-6
- 658 Flannigan, M., Cantin, A. S., De Groot, W. J., Wotton, M., Newbery, A., &  
 659 Gowman, L. M. (2013). Global wildland fire season severity in the 21st  
 660 century. *Forest Ecology and Management*, 294, 54–61. doi: 10.1016/  
 661 j.foreco.2012.10.022
- 662 Gharaylou, M., Farahani, M. M., Mahmoudian, A., & Hosseini, M. (2020). Pre-  
 663 diction of lightning activity using WRF-ELEC model: Impact of initial and

- 664 boundary conditions. *Journal of Atmospheric and Solar-Terrestrial Physics*,  
665 *210*, 105438. doi: 10.1016/j.jastp.2020.105438
- 666 Gilliland, E. K., & Rowe, C. M. (2007). A comparison of cumulus parameterization  
667 schemes in the WRF model. *87th AMS Annual Meeting*(Arakawa).
- 668 Grell, G. A., & Dévényi, D. (2002). A generalized approach to parameterizing con-  
669 vection combining ensemble and data assimilation techniques. *Geophysical Re-*  
670 *search Letters*, *29*, 34–38. doi: <https://doi.org/10.1029/2002gl015311>
- 671 He, J., & Loboda, T. V. (2020). Modeling cloud-to-ground lightning probability  
672 in Alaskan tundra through the integration of Weather Research and Forecast  
673 (WRF) model and machine learning method. *Environmental Research Letters*,  
674 *15*(11). doi: 10.1088/1748-9326/abbc3b
- 675 Helbig, M., Waddington, J. M., Alekseychik, P., Amiro, B., Aurela, M., Barr, A. G.,  
676 ... Schulze, C. (2020). The biophysical climate mitigation potential of boreal  
677 peatlands during the growing season. *Environmental Research Letters*, *15*(10).  
678 doi: 10.1088/1748-9326/abab34
- 679 Hoyer, J. L., Le Brogne, P., & Eastwood, S. (2014). A bias correction method for  
680 Arctic satellite sea surface temperature observations. *Remote Sensing of Envi-*  
681 *ronment*, *146*. doi: <https://doi.org/10.1016/j.rse.2013.04.020>
- 682 Iguchi, T., Tao, W. K., Wu, D., Peters-Lidard, C., Santanello, J. A., Kemp, E., ...  
683 Loikith, P. (2017). Sensitivity of CONUS summer rainfall to the selection of  
684 cumulus parameterization schemes in NU-WRF seasonal simulations. *Journal*  
685 *of Hydrometeorology*, *18*(6), 1689–1706. doi: 10.1175/JHM-D-16-0120.1
- 686 Krawchuk, M. A., Cumming, S. G., & Flannigan, M. D. (2009). Predicted changes  
687 in fire weather suggest increases in lightning fire initiation and future area  
688 burned in the mixedwood boreal forest. *Climatic Change*, *92*(1-2), 83–97. doi:  
689 10.1007/s10584-008-9460-7
- 690 Kumar, S. V., Peters-Lidard, C. D., Tian, Y., Houser, P. R., Geiger, J., Olden, S.,  
691 ... Sheffield, J. (2006). Land information system: An interoperable frame-  
692 work for high resolution land surface modeling. *Environmental Modelling and*  
693 *Software*, *21*(10), 1402–1415. doi: 10.1016/j.envsoft.2005.07.004
- 694 Kumar, S. V., Reichle, R. H., Peters-Lidard, C. D., Koster, R. D., Zhan, X., Crow,  
695 W. T., ... Houser, P. R. (2008). A land surface data assimilation framework  
696 using the land information system: Description and applications. *Advances in*  
697 *Water Resources*, *31*(11), 1419–1432. doi: 10.1016/j.advwatres.2008.01.013
- 698 Lang, S. E., Tao, W. K., Chern, J. D., Wu, D., & Li, X. (2014). Benefits of a fourth  
699 ice class in the simulated radar reflectivities of convective systems using a bulk  
700 microphysics scheme. *Journal of the Atmospheric Sciences*, *71*(10), 3583–3612.  
701 doi: 10.1175/JAS-D-13-0330.1
- 702 Loisel, J., Gallego-Sala, A. V., Amesbury, M. J., Magnan, G., Anshari, G., Beil-  
703 man, D. W., ... Wu, J. (2021). Expert assessment of future vulnerability of  
704 the global peatland carbon sink. *Nature Climate Change*, *11*(1), 70–77. doi:  
705 10.1038/s41558-020-00944-0
- 706 Lucas-Picher, P., Argüeso, D., Brisson, E., Trambly, Y., Berg, P., Lemonsu, A., ...  
707 Caillaud, C. (2021, 11). Convection-permitting modeling with regional climate  
708 models: Latest developments and next steps. *WIREs Climate Change*, *12*. doi:  
709 10.1002/wcc.731
- 710 Lynn, B., & Yair, Y. (2010). Prediction of lightning flash density with the WRF  
711 model. *Advances in Geosciences*, *23*(February), 11–16. doi: 10.5194/adgeo-23  
712 -11-2010
- 713 Madala, S., Satyanarayana, A. N. V., & Rao, T. N. (2014). Performance evalua-  
714 tion of PBL and cumulus parameterization schemes of WRF ARW model in  
715 simulating severe thunderstorm events over Gadanki MST radar facility - Case  
716 study. *Atmospheric Research*, *139*, 1–17. doi: 10.1016/j.atmosres.2013.12.017
- 717 Mason, B., & Dash, J. G. (2000). Charge and mass transfer in ice-ice collisions: Ex-  
718 perimental observations of a mechanism in thunderstorm electrification. *Jour-*

- 719 *nal of Geophysical Research*, *105*, 10185-10192.
- 720 McCaul, E. W., Goodman, S. J., LaCasse, K. M., & Cecil, D. J. (2009). Forecasting  
721 lightning threat using cloud-resolving model simulations. *Weather and Fore-*  
722 *casting*, *24*(3), 709–729. doi: 10.1175/2008WAF2222152.1
- 723 Mellor, G. L., & Yamada, T. (1982). Development of a turbulence closure model for  
724 geophysical fluid problems. *Reviews of Geophysics*, *20*, 851. doi: https://doi  
725 .org/10.1029/rg020i004p00851
- 726 Melton, J., Arora, V., Wisernig-Cojoc, E., Seiler, C., Fortier, M., Chan, E., & Teck-  
727 entrup, L. (2019). CLASSIC v1.0: the open-source community successor  
728 to the Canadian Land Surface Scheme (CLASS) and the Canadian Terres-  
729 trial Ecosystem Model (CTEM) – Part 1: Model framework and site-level  
730 performance. *Geoscientific Model Development Discussions*, 1–40. doi:  
731 10.5194/gmd-2019-329
- 732 NASA. (2020). NU-WRF Version 10 User ’ s Guide.
- 733 Newton, C. W. (1950). STRUCTURE AND MECHANISM OF THE PRE-  
734 FRONTAL SQUALL LINE. *Journal of Atmospheric Sciences*, *7*(3), 210–222.  
735 doi: 10.1175/1520-0469(1950)007(0210:SAMOTP)2.0.CO;2
- 736 Niu, G. Y., Yang, Z. L., Mitchell, K. E., Chen, F., Ek, M. B., Barlage, M., . . . Xia,  
737 Y. (2011). The community Noah land surface model with multiparameteriza-  
738 tion options (Noah-MP): 1. Model description and evaluation with local-scale  
739 measurements. *Journal of Geophysical Research Atmospheres*, *116*(12), 1–19.  
740 doi: 10.1029/2010JD015139
- 741 Perkins, S. E., Pitman, A. J., Holbrook, N. J., & McAneney, J. (2007). Evaluation  
742 of the AR4 Climate Models’ Simulated Daily Maximum Temperature, Mini-  
743 mum Temperature, and Precipitation over Australia Using Probability Density  
744 Functions. *Journal of Climate*, *20*(17), 4356–4376. doi: 10.1175/JCLI4253.1
- 745 Peters-Lidard, C. D., Kemp, E. M., Matsui, T., Santanello, J. A., Kumar, S. V.,  
746 Jacob, J. P., . . . Zupanski, M. (2015). Integrated modeling of aerosol, cloud,  
747 precipitation and land processes at satellite-resolved scales. *Environmental*  
748 *Modelling and Software*, *67*, 149–159. doi: 10.1016/j.envsoft.2015.01.007
- 749 Prein, A. F., Gobiet, A., Suklitsch, M., Truhetz, H., Awan, N. K., Keuler, K.,  
750 & Georgievski, G. (2013). Added value of convection permitting sea-  
751 sonal simulations. *Climate Dynamics*, *41*(9-10), 2655–2677. doi: 10.1007/  
752 s00382-013-1744-6
- 753 Prein, A. F., Langhans, W., Fosser, G., Ferrone, A., Ban, N., Goergen, K., . . . Le-  
754 ung, R. (2015). A review on regional convection-permitting climate modeling:  
755 Demonstrations, prospects, and challenges. *Reviews of Geophysics*, *53*(2),  
756 323–361. doi: 10.1002/2014RG000475
- 757 Price, C., & Rind, D. (1992). A Simple Lightning Parameterization for Calculating  
758 Global Lightning Distributions. , *97*(92), 9919–9933.
- 759 Price, C., & Rind, D. (1994). Modeling Global Lightning Distributions in a General  
760 Circulation Model. *Monthly Weather Review*, *122*, 1930–1939. doi: 10.1175/  
761 1520-0493(1994)122(1930:mglidia)2.0.co;2
- 762 Qiu, C., Zhu, D., Ciais, P., Guenet, B., Krinner, G., Peng, S., . . . Ziemblinska, K.  
763 (2018). ORCHIDEE-PEAT (revision 4596), a model for northern peatland  
764 CO<sub>2</sub>, water, and energy fluxes on daily to annual scales. *Geoscientific Model*  
765 *Development*, *11*(2), 497–519. doi: 10.5194/gmd-11-497-2018
- 766 Reynolds, S. E., Brook, M., & Gourley, M. F. (1957). Thunderstorm charge sepa-  
767 ration. *Journal of Atmospheric Sciences*, *14*(5), 426 - 436. doi: 10.1175/1520  
768 -0469(1957)014(0426:TCS)2.0.CO;2
- 769 Roebber, P. J. (2009). Visualizing multiple measures of forecast quality. *Weather*  
770 *and Forecasting*, *24*(2), 601–608. doi: 10.1175/2008WAF2222159.1
- 771 Romps, D. M., Charn, A. B., Holzworth, R. H., Lawrence, W. E., Molinari, J., &  
772 Vollaro, D. (2018). CAPE Times P Explains Lightning Over Land But Not the  
773 Land-Ocean Contrast. *Geophysical Research Letters*, *45*(22), 12,612–623,630.

- 774 doi: 10.1029/2018GL080267
- 775 Romps, D. M., Seeley, J. T., Vollaro, D., & Molinari, J. (2014). Projected in-  
776 crease in lightning strikes in the united states due to global warming. *Science*,  
777 *346*(6211), 851–854. doi: 10.1126/science.1259100
- 778 Santanello, J. A., Kumar, S. V., Peters-Lidard, C. D., Harrison, K., & Zhou, S.  
779 (2013). Impact of land model calibration on coupled land-atmosphere pre-  
780 diction. *Journal of Hydrometeorology*, *14*(5), 1373–1400. doi: 10.1175/  
781 JHM-D-12-0127.1
- 782 Sarmadi, F., Huang, Y., Thompson, G., Siems, S. T., & Manton, M. J. (2019).  
783 Simulations of orographic precipitation in the Snowy Mountains of South-  
784 eastern Australia. *Atmospheric Research*, *219*(January), 183–199. Re-  
785 trieved from <https://doi.org/10.1016/j.atmosres.2019.01.002> doi:  
786 10.1016/j.atmosres.2019.01.002
- 787 Saunders, C. (2008). Charge separation mechanisms in clouds. , 335–353.
- 788 Scharlemann, J. P. W., Tanner, E. V. J., Hiederer, R., & Kapos, V. (2014). Global  
789 soil carbon: Understanding and managing the largest terrestrial carbon pool.  
790 *Carbon Management*, *5*(1), 81–91. doi: 10.4155/cmt.13.77
- 791 Skamarock, W. C., Klemp, J. B., Dudhi, J., Gill, D. O., Barker, D. M., Duda,  
792 M. G., ... Powers, J. G. (2008). A Description of the Advanced Research  
793 WRF Version 3. *Technical Report*(June), 113. doi: 10.5065/D6DZ069T
- 794 Smith, R. B. (1979). The influence of mountains on the atmosphere. In B. Saltz-  
795 man (Ed.), (Vol. 21, p. 87-230). Elsevier. doi: [https://doi.org/10.1016/S0065-](https://doi.org/10.1016/S0065-2687(08)60262-9)  
796 [-2687\(08\)60262-9](https://doi.org/10.1016/S0065-2687(08)60262-9)
- 797 Takahashi, T. (1978). Riming electrification as a charge generation mechanism in  
798 thunderstorms. *Journal of Atmospheric Sciences*, *35*(8), 1536 - 1548. doi: 10  
799 .1175/1520-0469(1978)035(1536:REAACG)2.0.CO;2
- 800 Tao, W. K., Lang, S., Zeng, X., Li, X., Matsui, T., Mohr, K., ... Yang, Y. M.  
801 (2014). The Goddard Cumulus Ensemble model (GCE): Improvements and  
802 applications for studying precipitation processes. *Atmospheric Research*, *143*,  
803 392–424.
- 804 Tao, W. K., Wu, D., Lang, S., Chern, J. D., Peters-Lidard, C., Fridlind, A.,  
805 & Matsui, T. (2016). High-resolution NU-WRF simulations of a deep  
806 convective-precipitation system during MC3E: Further improvements and  
807 comparisons between Goddard microphysics schemes and observations.  
808 *Journal of Geophysical Research: Atmospheres*, *121*, 1278–1305. doi:  
809 10.1002/2015JD023986.Received
- 810 Tao, Z., Chin, M., Gao, M., Kucsera, T., Kim, D., Bian, H., ... Akimoto, H. (2020).  
811 Evaluation of NU-WRF model performance on air quality simulation under  
812 various model resolutions - An investigation within the framework of MICS-  
813 Asia Phase III. *Atmospheric Chemistry and Physics*, *20*(4), 2319–2339. doi:  
814 10.5194/acp-20-2319-2020
- 815 Thompson, G., Field, P. R., Rasmussen, R. M., & Hall, W. D. (2008). Explicit Fore-  
816 casts of Winter Precipitation Using an Improved Bulk Microphysics Scheme.  
817 Part II: Implementation of a New Snow Parameterization. *Monthly Weather*  
818 *Review*, *136*(12), 5095–5115. doi: 10.1175/2008MWR2387.1
- 819 Turetsky, M. R., Benscoter, B., Page, S., Rein, G., Van Der Werf, G. R., & Watts,  
820 A. (2015). Global vulnerability of peatlands to fire and carbon loss. *Nature*  
821 *Geoscience*, *8*(1), 11–14. doi: 10.1038/ngeo2325
- 822 Ushio, T., Heckman, S. J., Boccippio, D. J., Christian, H. J., & Kawasaki, Z. I.  
823 (2001). A survey of thunderstorm flash rates compared to cloud top height  
824 using TRMM satellite data. *Journal of Geophysical Research Atmospheres*,  
825 *106*(D20), 24089–24095. doi: 10.1029/2001JD900233
- 826 Vanden Broucke, S., & Van Lipzig, N. (2017). Do convection-permitting models  
827 improve the representation of the impact of LUC? *Climate Dynamics*, *49*(7),  
828 2749–2763. doi: 10.1007/s00382-016-3489-5

- 829 Veraverbeke, S., Rogers, B. M., Goulden, M. L., Jandt, R. R., Miller, C. E., Wig-  
830 gins, E. B., & Randerson, J. T. (2017). Lightning as a major driver of recent  
831 large fire years in North American boreal forests. *Nature Climate Change*,  
832 7(7), 529–534. doi: 10.1038/nclimate3329
- 833 Weisman, M. L., Skamarock, W. C., & Klemp, J. B. (1997). The resolution de-  
834 pendence of explicitly modeled convective systems. *Monthly Weather Review*,  
835 125(4), 527–548. doi: 10.1175/1520-0493(1997)125<0527:TRDOEM>2.0.CO;2
- 836 Wentz, F., Mears, C., Meissner, T., Ricciardulli, L., Lindsley, R., Manaster, A.,  
837 ... Wentz, K. (2016). *Monthly Mean Wind Speed Data Set on a 1 degree*  
838 *grid made from Remote Sensing Systems Version-7 Microwave Radiometer*  
839 *Data, V0701* [dataset]. Santa Rosa, CA, USA. Retrieved 2020-10-01, from  
840 [www.remss.com](http://www.remss.com)
- 841 Wong, J., Barth, M. C., & Noone, D. (2013). Evaluating a lightning parame-  
842 terization based on cloud-top height for mesoscale numerical model simu-  
843 lations. *Geoscientific Model Development*, 6(2), 429–443. doi: 10.5194/  
844 gmd-6-429-2013
- 845 Wotton, B. M., Nock, C. A., & Flannigan, M. D. (2010). Forest fire occurrence and  
846 climate change in Canada. *International Journal of Wildland Fire*, 19(3), 253–  
847 271. doi: 10.1071/WF09002
- 848 Yair, Y., Lynn, B., Price, C., Kotroni, V., Lagouvardos, K., Morin, E., ... Del Car-  
849 men Llasat, M. (2010). Predicting the potential for lightning activity in  
850 Mediterranean storms based on the Weather Research and Forecasting (WRF)  
851 model dynamic and microphysical fields. *Journal of Geophysical Research*  
852 *Atmospheres*, 115(4), 1–13. doi: 10.1029/2008JD010868
- 853 Yang, Z. L., Niu, G. Y., Mitchell, K. E., Chen, F., Ek, M. B., Barlage, M., ...  
854 Xia, Y. (2011). The community Noah land surface model with mul-  
855 tiparameterization options (Noah-MP): 2. Evaluation over global river  
856 basins. *Journal of Geophysical Research Atmospheres*, 116(12), 1–16. doi:  
857 10.1029/2010JD015140
- 858 Yoshida, S., Morimoto, T., Ushio, T., & Kawasaki, Z. I. (2009). A fifth-power  
859 relationship for lightning activity from Tropical Rainfall Measuring Mission  
860 satellite observations. *Journal of Geophysical Research Atmospheres*, 114(9),  
861 1–10. doi: 10.1029/2008JD010370